Imaging Energy-, Momentum-, and Time-Resolved Distributions of Photoinjected Hot Electrons in GaAs

Jun'ichi Kanasaki, Hiroshi Tanimura, and Katsumi Tanimura
The Institute of Scientific and Industrial Research, Osaka University, 8-1 Mihogaoka, Ibaraki, Osaka 567-0047, Japan
(Received 2 July 2014; published 2 December 2014)

Using time-and angle-resolved photoemission spectroscopy, we determine directly energy-, momentum-, and time-resolved distributions of hot electrons photoinjected into the conduction band of GaAs, a prototypical direct-gap semiconductor. The nascent distributions of photoinjected electrons are captured for different pump photon energies and polarization. The evolutions of hot electron distributions in ultrafast intervalley scattering processes are resolved in momentum space with fs-temporal resolution, revealing an intervalley transition time as short as 20 fs.

DOI: 10.1103/PhysRevLett.113.237401 PACS numbers: 78.47.db, 78.47.J-, 79.60.Bm

Ultrafast scattering of highly energetic carriers in semiconductors is the key process that ultimately determines functional limits and properties of micro- and optoelectronics, being a strategic research field in the past two decades [1,2]. For over 40 years ultrafast optical spectroscopy has been developed that complements the transport measurements by capturing scattering dynamics. Despite accumulating knowledge, a clear understanding of the physics involved in dynamic scattering processes remains elusive due to the high complexity of the problem [1,2]. In addition, a greater understanding of scattering processes over the whole Brillouin zone has become critically important as current dimensions of nanoscale devices are comparable to carrier scattering lengths where fundamental quantum-mechanical scatterings determine key electronic properties [3–5].

Transient electron distribution functions (EDF's) provide the key information necessary to elucidating incoherent scattering dynamics [2]. In fact, EDF's experimentally determined so far provided deeper insight into the processes, e.g., electronic thermalization of hot electrons [6], transient electron velocity overshoot in nanostructured semiconductors [7], and intravalley hot-electron relaxation in Si [8]. However, directly determined transient EDF's are rare in ultrafast scattering processes. In most cases, they have been inferred indirectly, using theoretical modeling [9–11]. Because many assumptions and approximations are used in the modeling, an understanding of several important scattering processes still remains incomplete [1].

Ultrafast intervalley scattering (IVS) of hot electrons in semiconductors is one such issue to be explored using directly determined EDF's. Intervalley scattering in GaAs has been studied extensively using various optical techniques. However, reported transition times range from 80 to 540 fs for Γ-to-L scattering [12–16]. The wide dispersion of reported transition times and strong dependence on excitation density and temperature [14,15] have yet to be reconciled. Although decay times on the order of a few tens of fs in optical signals have been ascribed to the IVS [17–20], the details of the scattering processes and mechanisms have not been elucidated thoroughly.

Here we report a new methodology to determine transient EDF's resolved in energy and momentum spaces with fs-temporal resolution. Using time- and angle-resolved photoemission spectroscopy, we capture directly the nascent photoinjected-electron distributions in the conduction band (CB) of GaAs. Furthermore, by resolving fs-temporal changes in EDF's, we reveal important features of ultrafast IVS of hot electrons.

Zn-doped p-type GaAs (110) wafers with resistivity of 4.8 Ω cm were cleaved under ultrahigh vacuum conditions ($<5 \times 10^{-11}$ Torr). Surface structures were characterized *in situ* by a scanning tunneling microscope prior to photoemission measurements [21]. A laser system, consisting of a Ti-sapphire laser oscillator, a regenerative amplifier, and a tunable optical parametric amplifier, generated 50-fs laser pulses centered at photon energies between 1.7 to 2.4 eV. A part of the amplified fundamental output at 824 nm was used to generate the 70-fs third harmonic pulses for probing photoemission. Pump and probe pulses, with a preset time delay (Δt), were aligned coaxially and focused on the sample surfaces at 45° to normal. A hemispherical electron analyzer operated in an angle-resolved lens mode, and a two-dimensional image-type detector served as the electron spectrometer. Photoelectron images were recorded as a function of kinetic energy and emission angle of photoelectrons. The energy resolution with fs-probe light was 50 meV, while angle resolution was $\pm 1°$.

Figure 1(a) displays the band diagram of GaAs [22–24]. Figures 1(b) and 1(c) show photoemission maps as a function of electron energy ε and emission angle θ, measured at $\Delta t = 20$ fs with s-and p-polarized 2.21 eV pump pulses, while Fig. 1(d) shows the map at $\Delta t = 10$ ps. The scale of ε is referenced to the conduction band minimum (CBM), which can be determined precisely based on data shown in Fig. 1(d). We abbreviate the photoemission

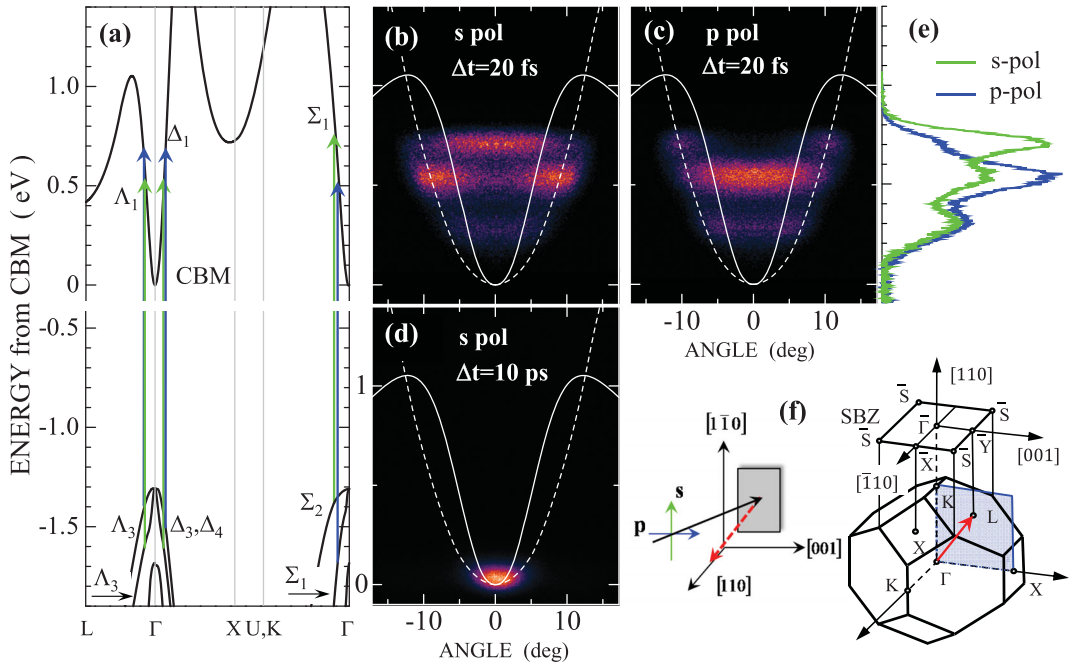

FIG. 1 (color). (a) A part of the band structure of GaAs (Ref. [22]). Energy is referenced to the conduction-band minimum. The symmetries of spatial parts of wave functions are given for the points involved in the interband transitions (Ref. [25]). Green (blue) arrows show typical allowed optical transitions for s-(p-) polarized 2.21-eV photons. (b) The image of photoelectrons 20 fs after excitation with s-polarized 2.21-eV light pulses. (c) The image of photoelectrons 20 fs after excitation with p-polarized 2.21-eV light pulses. (d) The image of photoelectrons 10 ps after excitation with s-polarized 2.21-eV light pulses. In (b), (c), and (d), the color scale indicates the photoemission intensity. (e) Normal photoemission spectra in the images in (b) and (c). The intensities at $\theta = 0 \pm 0.5°$ are integrated. (f) Experimental geometry of photoemission measurements, and the relation between the surface Brillouin zone and bulk Brillouin zone for GaAs with (110) surface under this geometry. The plane shown by light blue is the projection plane, and the red arrow within the plane shows the direction from the Γ to L points.

intensity as $I(\varepsilon, \theta, \Delta t)$, hereafter. For the pump-photon energy ($h\nu_{\text{pump}}$) of 2.21 eV, transitions from heavy-hole (HH), light-hole (LH), and split-off (SO) valence bands to the CB are possible. In fact, the normal emission spectra ($\theta = 0$) of the images in Figs. 1(b) and 1(c), as shown in Fig. 1(e), demonstrate that the initial states of photoemission, or the final states of photoexcitation, consist of three peaks at 0.71, 0.53, and 0.30 eV. The photoemission maps show highly polarization-dependent features in both intensity and angular distribution. Since the photoemission is probed using the same p-polarized 4.51-eV light, the polarization-dependent features reflect directly the photoexcitation processes.

As displayed in Fig. 1(f), the [110] crystal axis is aligned along the surface normal, and the [110] and [001] axes define the detection plane. The relation between the bulk Brillouin zone (BBZ) and the surface Brillouin zone (SBZ) is also shown under this geometry. As the emission angle θ corresponds to electron momentum ($k_{//}$) parallel to the surface along the $\bar{\Gamma}$-$\bar{Y}$ direction of the SBZ, the measured photoemission image represents a one-dimensional cut, along $\bar{\Gamma}$-$\bar{Y}$ of the SBZ, of the two-dimensional projection of three-dimensional electron distributions. The projection has the following characteristics. First, all states along the Γ-K direction in the BBZ are projected at $\bar{\Gamma}$, contributing to normal photoemission. Second, the states along the Γ-X in the BBZ are projected on the $\bar{\Gamma}$-$\bar{Y}$ direction with $k_{//} = k_X$. Third, the states along the Γ-L in the BBZ are projected on the $\bar{\Gamma}$-$\bar{Y}$ direction with $k_{//}$ given by $k_{//} = k_L \cos(54.7°)$. Here k_X and k_L are wave vectors along the Γ-X and Γ-L directions. The dispersion of the CB along the Γ-L and Γ-X directions is calculated as a function θ assuming a constant ionization potential (see Supplemental Material [26]), and plotted by the solid and broken curves in Figs. 1(b), 1(c), and 1(d).

The polarization selection rule [25] predicts that the transition from the HH (Σ_2) or LH (Σ_1) band at Σ is selectively allowed under s- or p-polarized excitation in the present geometry. In fact, the intensity around $k_{//} = 0$ for the highest-energy peak injected from the HH band is intense only for s-polarized light, while the intensity around $k_{//} = 0$ of the second-energy peak from the LH band is intense only for p-polarized light. For p-polarized light, the highest-energy peak shows maxima at $\theta = \pm 9°$, corresponding to $k_{//} = 1.2 \times 10^7$ cm^{-1} as in Fig. 1(c). The selection rule predicts allowed transitions from the HH band to the CB along Γ-X at $k_X = 1.36 \times 10^7$ cm^{-1}, in reasonable agreement with our result. For s-polarized light,

the peak from the LH band is detected at $\theta = \pm 7.5°$, which correspond to $k_{//} = 9.2 \times 10^6$ cm^{-1}. The selection rule predicts the transition at $k_L = 1.31 \times 10^7$ cm^{-1} along the Γ-L line, corresponding to $k_{//} = 7.57 \times 10^6$ cm^{-1}, and that at $k_X = 1.19 \times 10^7$ cm^{-1} along the Γ-X line. The overlap of the two transitions makes the angle distribution broader with the mean value of $k_{//} = 9.73 \times 10^6$ cm^{-1}, as we observe.

Figure 2(a) displays the angle-integrated spectra of $I(\varepsilon, \theta, 20\text{ fs})$ measured at $\Delta t = 20$ fs for s-polarized light with $h\nu_{\text{pump}}$ ranging from 1.7 to 2.3 eV. The solid, chain, and dotted curves in Fig. 2(a) show the predicted final-state energies in the CB for transitions from HH, LH, and SO bands around Σ. The observed peak energies agree reasonably well with the predicted energies [24]. Therefore, our photoemission spectroscopy captures directly the nascent distribution of photoinjected electrons in the bulk CB of GaAs.

Temporal changes in EDF's reflect directly hot-electron relaxation. To differentiate between relaxation pathways that critically depend on the excess energy ε, we analyzed the population dynamics of the highest-energy states, P_{HE} [34]. We evaluated P_{HE} by integrating $I(\varepsilon, \theta, \Delta t)$ over ε, larger than the energy specified by the black arrow indicated on each spectrum; the energy defines the point providing one half of the highest-energy peak intensity. Figure 2(b) shows the temporal changes of the P_{HE} for typical $h\nu_{\text{pump}}$'s. The optical Bloch equation [35], incorporated with a rate equation, was used to analyze the initial rise and population decay time T_1, shown by solid curves, and the persistent changes at longer Δt, shown by broken curves (see Supplemental Material for details [26]). At $h\nu_{\text{pump}} = 1.70$ eV, $T_1 = 165$ fs, and the decay is persistent over $\Delta t = 500$ fs. At $h\nu_{\text{pump}} = 1.8$ eV, the initial decay rate increases, with $T_1 = 40 \pm 3$ fs, and it increases further, to $T_1 = 22 \pm 3$ fs, for $h\nu_{\text{pump}}$ above 2.10 eV. In Fig. 2(a), experimental results of minimum energies at L (E_L) and X (E_X) valleys [23] are indicated by arrows. Taking our finite energy resolution of 50 meV into account, a substantial fraction of P_{HE} at $h\nu_{\text{pump}} = 1.70$ eV comes from states below E_L, while all states for P_{HE} at $h\nu_{\text{pump}} = 1.80$ eV are above E_L, but below E_X. On the other hand, at $h\nu_{\text{pump}} = 2.21$ eV, all states contributing to P_{HE} are above E_X. Therefore, ultrafast decay channels become active at ε above E_L.

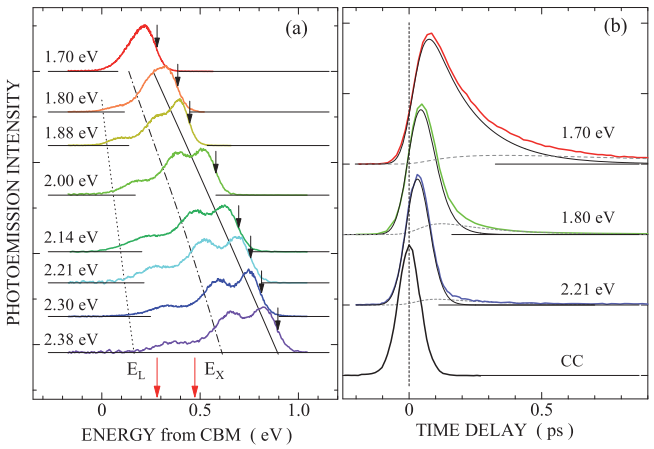

FIG. 2 (color). (a) Angle-integrated photoemission spectra, measured at $\Delta t = 20$ fs, excited by s-polarized light pulses with photon energies ranging from 1.70 to 2.38 eV. Excitation density ρ is typically $\lesssim 5 \times 10^{17}$ cm^{-3}. (b) Temporal change of population at the highest-energy states of the spectra (for definition see the text) for excitation photon energies of 1.70 eV ($\rho = 4.7 \times 10^{17}$ cm^{-3}), 1.80 eV ($\rho = 4.5 \times 10^{17}$ cm^{-3}), and 2.21 eV ($\rho = 3.2 \times 10^{17}$ cm^{-3}). The solid curves show the best-fit solutions of the optical Bloch equation, while the dashed curves display rate-equation results that incorporate cascade effects of relaxation. The black curve, labeled CC, displays the cross-correlation trace between pump and probe pulses.

The dynamics of ultrafast decay of hot electrons was studied by measuring time-, energy-, and angle-resolved EDF's under $h\nu_{\text{pump}} = 2.30$ eV at excitation density $\rho = 3.5 \times 10^{17}$ cm^{-3}. Figure 3(a) displays a map of angle-integrated intensity over $\pm 15°$ as a function of Δt and ε, showing temporal evolution of EDF's in the Γ valley. The spectra of angle-integrated EDF's in the first 200 fs are shown in Fig. 3(b); the population above E_X is lost rapidly. To quantify the changes in total population in the Γ valley,

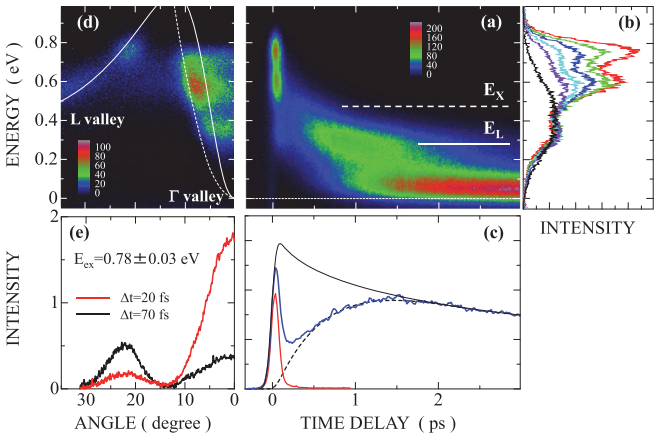

FIG. 3 (color). (a) The photoemission map for hot electrons in the Γ valley injected by 2.30-eV light pulses as a function of energy and Δt. The solid and broken lines labeled E_L and E_X show the experimental values of L-and X-valley minima. (b) Red, green, blue, light blue, and violet curves show angle integrated distribution functions measured at 20-fs intervals of Δt from 20 to 100 fs in order, and the black curve shows the function at $\Delta t = 200$ fs. (c) Temporal changes of the total photoemission intensity integrated over ε and θ, (blue line), and of the population at the highest-energy states, (red line), as a function of Δt. The solid black curve shows the result of analysis by the diffusion equation, and the broken curve is the best fit of the rate equation model with the restoration of the total intensity. (d) The image of photoelectrons 70 fs after excitation with 2.30-eV s-polarized light. The color scale indicates the relative photoemission intensity. (e) Photoemission intensities at $\varepsilon = 0.78 \pm 0.3$ eV as a function of θ for $\Delta t = 20$ fs (red line), and 70 fs (black line).

the total photoelectron intensity, $I(\varepsilon, \theta, \Delta t)$ integrated over ε and θ, are plotted (blue curve) as a function of Δt in Fig. 3(c). The intensity is rapidly quenched within $\Delta t = 200$ fs, but is restored again by $\Delta t = 1$ ps. The restoration between 0.3 to 1.5 ps can be approximated by a time constant of 0.77 ps, as shown by the broken curve. To examine the possible effects of carrier diffusion from our probed region (~10 nm from the surface) into the bulk, we calculated the diffusion rate, using an absorption coefficient at 2.30 eV [36] and an ambipolar diffusion constant [37]. As shown by the solid curve in Fig. 3(c), the carrier diffusion rate is slow, compared with the rapid quenching of the total intensity, confirming that the ultrafast loss in the Γ-valley population is due to IVS. Therefore, our result in Fig. 3(c) displays temporal changes in total hot-electron population in the Γ valley for a whole process, including photoinjection of hot electrons, their escape from the Γ valley and the back scattering into the Γ valley. Importantly, our direct determination of EDF's provides further insight into the IVS process.

First, we can capture directly the hot electrons scattered into the L valley. Figure 3(d) displays photoemission maps for θ from 0 to 35°, measured at $\Delta t = 70$ fs. In the map, the dispersions of the CB along Γ-L and Γ-X directions are shown by solid and broken curves as in Fig. 1. At $\Delta t = -30$ fs, only the photoinjected populations in the Γ valley are detectable, while finite populations in the L valley ($\theta > 15°$) are clearly detected at $\Delta t = 70$ fs. In Fig. 3(e), photoemission intensities at $\varepsilon = 0.78 \pm 0.3$ eV, near the peak energy for electrons photoinjected from the HH band, are plotted as a function of θ for $\Delta t = 20$ and 70 fs. As the Γ-valley intensity decreases, the L-valley intensity increases concurrently. The rise time of the L-valley population is identical to the decay time of the Γ-valley population given by $T_1 (= 22 \pm 3$ fs), probing directly Γ-to-L scattering. The L-valley distribution at $\Delta t = 70$ fs shows a peak at $\theta = 22°$, which corresponds to $k_L = 5.43 \times 10^7$ cm^{-1}, defining the wave vector of intervalley phonons. As $\varepsilon = 0.78$ eV is higher than E_X, scattering into the X valley may also be induced [14,15,18]. Therefore, T_1 corresponds to the total transition rates into both the X and L valleys.

Second, the results in Fig. (3) provide a unique feature of ultrafast IVS. As seen in Fig. 3(b), during IVS, the three-peak structure in the nonequilibrium distribution in the Γ valley is maintained even at $\Delta t \sim 200$ fs. An ensemble Monte Carlo study reported that the presence of e-e scattering modifies both population transition rates and carrier densities in the satellite valleys, primarily by reshaping the energy distribution of carriers in the Γ valley [38]. However, the ultrafast IVS in the present case is not associated with such energy redistributions of hot electrons in the Γ valley even for $\rho = 3.5 \times 10^{17}$ cm^{-3}.

Importantly, our results have proven that IVS takes place with a time constant as short as ~20 fs for hot electrons with $\varepsilon > 0.7$ eV. To obtain more insight into the mechanisms, we studied the effects of excitation density and temperature on T_1 under 2.21-eV excitation. Measurements for $\rho = 6 \times 10^{18}$ cm^{-3} at 293 K show that the nascent distribution is significantly broadened (see Supplemental Material [26]), but that $T_1 (21 \pm 3$ fs) is almost identical to that at $\rho = 3.2 \times 10^{17}$ cm^{-3}. In contrast, the magnitude of T_1 measured at 100 K is 30 ± 2 fs, such that the rate, as determined by $1/T_1$, becomes 73% of that measured at 293 K (see Supplemental Material [26]), suggesting some roles played by the electron-phonon interaction.

In previous studies, ultrafast IVS with scattering times less than 50 fs has been interpreted in terms of deformation potential interaction [39–41]. The intervalley phonons determined here for Γ-to-L scattering (zone-edge LO and LA phonons for Γ-to-X scattering [41]) have frequencies of typically 7.0 THz [42], the oscillation period of which is much longer than the transition time. Therefore, the ultrafast IVS process is in the quantum kinetics regime [41]. A rigorous analysis of temperature-dependent IVS rates revealed above, including wave-number-dependent deformation potentials of both LO and LA phonons [43] and the quantum aspects of the interaction [41], will give crucial information on the role of electron-phonon interaction in the ultrafast IVS process.

Within a few tens of fs after excitation, the electronic system evolves dynamically, governed by ultrafast processes including polarization dephasing [32] and the onset of collective behavior [44]. Bigot *et al.* have suggested that a unique electronic interaction specific to the short temporal domain after excitation is a possible mechanism of ultrafast IVS [20]. More generally, not only the electronic system but the lattice system evolves dynamically, triggered by coherent excitation of particular phonon modes [45]. Therefore, dynamical evolutions of both electronic and lattice systems may be associated with ultrafast IVS, on the order of 20 fs. We may define the transitions in the short temporal domain as the dynamical transition, characteristics of which are different from those under quasi-equilibrated conditions. This distinction could explain the significant differences in intervalley transition rates measured using different methods.

This work was supported by JSPS KAKENHI Grant Number 24000006.

[1] J. Shah, *Ultrafast Spectroscopy of semiconductors and Semiconductor Nanostructures*, 2nd ed. (Springer, Berlin, 1999).
[2] F. Rossi and T. Kuhn, Rev. Mod. Phys. **74**, 895 (2002).
[3] R. P. Prasankumar, P. C. Upadhya, and A. J. Taylor, Phys. Status Solidi B **246**, 1973 (2009).
[4] B. Fischer and K. R. Hofmann, Appl. Phys. Lett. **76**, 583 (2000).

[5] M. Hase, M. Kitajima, A. M. Constantinescu, and H. Petek, Nature (London) **426**, 51 (2003).
[6] D. W. Snoke, W. W. Rühle, Y.-C. Lu, and E. Bauser, Phys. Rev. B **45**, 10 979 (1992).
[7] E. D. Grann, K. T. Tsen, O. F. Sankey, D. K. Ferry, A. Salvador, A. Botcharev, and H. Morkoç, Appl. Phys. Lett. **67**, 1760 (1995).
[8] T. Ichibayashi and K. Tanimura, Phys. Rev. Lett. **102**, 087403 (2009).
[9] J. Zimmermann, P. Lugi, and D. K. Ferry, Solid State Electron. **26**, 233 (1983).
[10] M. A. Osman and D. K. Ferry, Phys. Rev. B **36**, 6018 (1987).
[11] L. Rota, P. Lugli, T. Elsaesser, and J. Shah, Phys. Rev. B **47**, 4226 (1993).
[12] K. Kash, P. A. Wolff, and W. A. Bonner, Appl. Phys. Lett. **42**, 173 (1983).
[13] J. Shah, B. Deveaud, T. C. Damen, W. T. Tsang, A. C. Gossard, and P. Lugli, Phys. Rev. Lett. **59**, 2222 (1987).
[14] P. C. Becker, H. L. Fragnito, C. H. Brito Cruz, J. Shah, R. L. Fork, J. E. Cunningham, J. E. Henry, and C. V. Shank, Appl. Phys. Lett. **53**, 2089 (1988).
[15] R. G. Ulbrich, J. A. Kash, and J. C. Tsang, Phys. Rev. Lett. **62**, 949 (1989).
[16] G. Fasol, W. Hackenberg, H. P. Hughes, K. Ploog, E. Bauser, and H. Kano, Phys. Rev. B **41**, 1461 (1990).
[17] W. Z. Lin, L. G. Fujimoto, E. P. Ippen, and R. A. Logan, Appl. Phys. Lett. **50**, 124 (1987).
[18] D. N. Mirlin, I. Ya. Karlik, and V. F. Sapega, Solid State Commun. **65**, 171 (1988).
[19] C. L. Tang, F. W. Wise, and I. A. Walmsley, Solid State Electron. **31**, 439 (1988).
[20] J.-Y. Bigot, M. T. Portella, R. W. Schoenlein, J. E. Cunningham, and C. V. Shank, Phys. Rev. Lett. **65**, 3429 (1990).
[21] J. Kanasaki, E. Inami, and K. Tanimura, Surf. Sci. **601**, 2367 (2007).
[22] B. D. Malone and M. L. Cohen, J. Phys. Condens. Matter **25**, 105503 (2013).
[23] I. Vurgaftman, J. R. Meyer, and L. R. Ram-Mohan, J. Appl. Phys. **89**, 5815 (2001).
[24] Even in the latest first-principles band-structure calculation in Ref. [22], quantitative agreement of the calculated energies with experimental values is not excellent; the comparison remains semiquantitative. Theory gives the band-gap energy at Γ to be 1.31 eV, which is smaller by 0.21 eV (0.116 eV) than the experimental value at 4 K (293 K). In evaluating transition energies and wave vectors for a given pump-photon energy, we artificially sifted the calculated conduction-band energy by 0.116 eV to have the same band-gap energy as the experimental value of 1.426 eV at 293 K.
[25] D. W. Niles, D. Rioux, and H. Höchst, Phys. Rev. B **46**, 12 547 (1992).
[26] See Supplemental Material at http://link.aps.org/supplemental/10.1103/PhysRevLett.113.237401, which includes Refs. [27–33].
[27] C. Eickhoff, M. Teichmann, and M. Weinelt, Phys. Rev. Lett. **107**, 176804 (2011).
[28] M. Kutschera, M. Weinelt, M. Rohlfing, and Th. Fauster, Appl. Phys. A **88**, 519 (2007).
[29] H. Haug and S. W. Koch, *Quantum Theory of the Optical and Electronic Properties of Semiconductors* (World Scientific, Singapore, 1990).
[30] M. J. Weida, S. Ogawa, H. Nagano, and H. Petek, J. Opt. Soc. Am. B **17**, 1443 (2000).
[31] T. Hertel, E. Knoesel, M. Wolf, and G. Ertl, Phys. Rev. Lett. **76**, 535 (1996).
[32] P. C. Becker, H. L. Fragnito, C. H. Brito Cruz, R. L. Fork, J. E. Cunningham, J. E. Henry, and C. V. Shank, Phys. Rev. Lett. **61**, 1647 (1988).
[33] A. Leitenstorfer, A. Lohner, T. Elsaesser, S. Haas, F. Rossi, T. Kuhn, W. Klein, G. Boehm, G. Traenkle, and G. Weimann, Phys. Rev. Lett. **73**, 1687 (1994).
[34] Changes in population at each state are complex, as they are governed not only by depletion of the initial population but also by population increase due to cascade processes during relaxation. However, the dynamics of population P_{HE} at the highest energy states can be analyzed with the least complexity, since the incoming flow is minimal.
[35] M. Schubert and B. Wilhelmi, *Nonlinear Optics and Quantum Electronics*, (John Wiley & Sons, New York, 1986).
[36] D. E. Aspnes and A. A. Studna, Phys. Rev. B **27**, 985 (1983).
[37] Diffusion coefficients of electrons and holes in GaAs were taken from the electronic archive of the Ioffe Physico-Technical Institute, http://www.ioffe.rssi.ru/SVA/NSM/.
[38] M. J. Kann, A. M. Kriman, and D. K. Ferry, Phys. Rev. B **41**, 12 659 (1990).
[39] D. W. Bailey, C. J. Stanton, M. A. Artaki, K. Hess, F. W. Wise, and C. J. Tang, Solid State Electron. **31**, 467 (1988).
[40] X. Zhou and T. Y. Hsiang, J. Appl. Phys. **67**, 7399 (1990).
[41] D. K. Ferry, A. M. Kriman, H. Hida, and S. Yamaguchi, Phys. Rev. Lett. **67**, 633 (1991).
[42] J. L. T. Waugh and G. Dolling, Phys. Rev. **132**, 2410 (1963).
[43] S. Zollner, S. Gopalan, and M. Cardona, J. Appl. Phys. **68**, 1682 (1990).
[44] R. Huber, F. Tauser, A. Brodschelm, M. Bichler, G. Abstreiter, and A. Leitenstorfer, Nature (London) **414**, 286 (2001).
[45] G. C. W. Cho, W. Kütt, and H. Kurz, Phys. Rev. Lett. **65**, 764 (1990).